The Astrophysical Journal, 889:33 (11pp), 2020 January 20 https://doi.org/10.3847/1538-4357/ab5e89

Population Synthesis of Helium White Dwarf–Red Giant Star Mergers and the Formation of Lithium-rich Giants and Carbon Stars

Xianfei Zhang[1], C. Simon Jeffery[2,3], Yaguang Li[1], and Shaolan Bi[1]
[1] Department of Astronomy, Beijing Normal University, Beijing, 100875, People's Republic of China; zxf@bnu.edu.cn
[2] Armagh Observatory, College Hill, Armagh BT61 9DG, UK
[3] School of Physics, Trinity College Dublin, Dublin 2, Ireland
Received 2019 September 11; revised 2019 November 11; accepted 2019 December 2; published 2020 January 22

Abstract

The formation histories of lithium-rich and carbon-rich red giants are not yet understood. It has been proposed that the merger of a helium-core white dwarf with a red giant branch (RGB) star might provide a solution. We have computed an extended grid of post-merger evolution models and combined these with predictions of binary-star population synthesis. The results strongly support the proposal that the merger of a helium white dwarf with an RGB star can provide the progenitors of both lithium-rich red clump stars and early-R carbon stars. The distribution of post-merger models in $T_{\rm eff}$, log g, log L, the surface abundances of lithium and carbon, and the predicted space densities agree well with the observed distributions of these parameters for Li-rich and early-R stars in the Galaxy.

Unified Astronomy Thesaurus concepts: Red giant stars (1372); Stellar physics (1621); Asteroseismology (73); Stellar abundances (1577); Red giant clump (1370); Stellar evolutionary models (2046); Stellar evolution (1599); Binary stars (154); White dwarf stars (1799); Lithium stars (927); Chemically peculiar stars (226); Carbon stars (199)

1. Introduction

Big Bang nucleosynthesis produced most of the observed lithium in the universe. Lithium is destroyed in stellar interiors once the temperature exceeds 2.5×10^6 K. Both theory (Iben 1967a, 1967b) and observations of globular cluster stars (Lind et al. 2009) show that surface lithium will be depleted during red giant branch (RGB) evolution to less than the solar surface value of $A(\mathrm{Li}) \equiv \log_{10}(N(\mathrm{Li})/N(\mathrm{H})) + 12 = 1.5$ due to the deep convective envelope in the first dredge-up stage. However, a small fraction of RGBs show a lithium-rich (Li-rich) photosphere ($\leqslant$1% in the Galactic disk; Brown et al. 1989). Hundreds of Li-rich giants have been found in the last few years, including tens of super Li-rich stars with $A(\mathrm{Li}) \geqslant 3.2$ (Kumar et al. 2011; Adamów et al. 2014; Casey et al. 2016; Deepak & Reddy 2019; Singh et al. 2019a; Zhou et al. 2019). The most Li-rich giant star so far discovered has $A(\mathrm{Li}) = 4.5$ (Yan et al. 2018). Most such super Li-rich giants are identified as red clump stars. Since red clump stars are core-helium-burning stars, they should have already passed through the first RGB where most of their surface lithium would have been destroyed (Carlberg et al. 2015; Jofré et al. 2015; Bharat Kumar et al. 2018; Singh et al. 2019a, 2019b). As well as Li-rich giants observed as field stars, some have been found in clusters (Carlberg et al. 2015), and in metal-poor populations (Li et al. 2018). Thus, the formation of Li-rich giants does not depend on special initial conditions but remains a puzzle for stellar evolution theory.

Three principal scenarios have been proposed to explain the lithium enrichment in these cases. (1) The lithium has been gained from a brown dwarf or rocky planet companion that contains lithium (Ashwell et al. 2005; Aguilera-Gómez et al. 2016). (2) Lithium-rich material has been accreted from an asymptotic giant branch (AGB) star or a nova companion (José & Hernanz 1998). (3) The lithium has been produced in the interior of the star and lifted to the surface by enhanced extra-mixing (Cameron & Fowler 1971; Sackmann & Boothroyd 1999; Charbonnel & Balachandran 2000; Denissenkov & Herwig 2004; Yan et al. 2018). In scenarios (1) and (2), we may expect to observe some other elements from their companion. The typical upper limit for lithium enrichment by such means is $A(\mathrm{Li}) \leqslant 2.2$ (Aguilera-Gómez et al. 2016). In scenario (3), the fresh lithium is produced by the Cameron–Fowler mechanism (Cameron & Fowler 1971), in which lithium is created following the $^3\mathrm{He}(\alpha, \gamma)^7\mathrm{Be}$ reaction; beryllium is assumed to be transported to a cooler region where it is converted to lithium by β-decay ($^7\mathrm{Be}(e^-, \nu)^7\mathrm{Li}$). Thus, such a star should have a hot burning interior zone to create ^{7}Be and an extra-mixing convection zone to bring the ashes of nuclear activity to the surface while avoiding lithium destruction by proton capture. In this scenario (3), the actual mechanism that drives the extra-mixing plays an important role. Several have been proposed including rotation and internal instabilities. So far, details are lacking, and the frequency at which such mechanisms occur in red giants is not known.

Another type of star with a chemically peculiar surface is a carbon star. Carbon stars are normally classified as being one of spectral types N, R, and J (Secchi 1868; Fleming & Pickering 1908) and have $\mathrm{C/O} > 1$ by numbers in their atmospheres. The N-type and some cool R-type (late-R) carbon stars are recognized as the normal and most significant population of carbon stars. Their surface compositions can be reproduced by low-mass AGB nucleosynthesis models that have been carbon enriched by the third dredge-up and have s-process elements in their atmospheres (Zamora et al. 2009). The hot R-type stars (early-R stars) and J-type stars are different from normal carbon stars. Their surfaces are enriched in $^{13}\mathrm{C}(^{12}\mathrm{C}/^{13}\mathrm{C} < 15)$ as well as ^{12}C but without s-process enhancements (Dominy 1984; Zamora et al. 2009). The early-R stars have magnitudes similar to the red clump stars (Knapp et al. 2001). Most of the early-R stars are single stars. The J-type carbon stars show a high luminosity with a location close to the AGB on the Hertzsprung–Russell (HR) diagram, and have a

smaller ratio of $^{12}C/^{13}C$ and more lithium on the surface than early-R stars (Abia & Isern 2000).

In the standard stellar evolution theory it is difficult to obtain models of single stars with carbon-enriched surfaces unless they are in the thermally pulsing AGB stage or in the Wolf–Rayet stage of massive star evolution. The R-stars are likely in the red clump (core-helium-burning) phase and are too faint to be in either of those stages. The formation channel of early-R stars was unclear for a long time, until the proposal that they formed by binary-star mergers was supported by binary-star population synthesis (BSPS) calculations (Izzard et al. 2007). A further study with a full calculation of the post-merger evolution with details of stellar parameters and abundance further supported this channel (Zhang & Jeffery 2013). In this merger model, the early-R stars are formed by helium white dwarfs (HeWDs) that merge with an RGB star. Surface lithium is enriched during this merger process. This channel could also produce the single J-type carbon stars (Zhang & Jeffery 2013), though these stars could also be explained by pollution from a nova companion (Sengupta et al. 2013). Due to the character of Li-rich giant and early-R stars, i.e., red-giant-like stars with surfaces enriched in lithium and/or carbon with a low $^{12}C/^{13}C$ ratio, it seems likely that the HeWD+RGB merger channel can produce either or both of these of stellar types.

Piersanti et al. (2010) performed a three-dimensional smoothed particle hydrodynamics (3D SPH) simulation of a low-mass HeWD+RGB merger ($M_{\rm HeWD} \leqslant 0.2\ M_{\odot}$) that shows that no efficient helium burning occurred to dredge up carbon material to the surface. Zhang & Jeffery (2013) found similar results from their 1D post-merger calculation and also suggested that a higher-mass HeWD subducted into a low-core-mass red giant could produce carbon enrichment at the surface of the giant. However, only five models were investigated by Zhang & Jeffery (2013), which also adopted a much higher accretion rate than that indicated by the 3D SPH simulation.

To survey the products of HeWD+RGB mergers in a larger parameter space, we extended the study of Zhang & Jeffery (2013) by modifying the model of the merger process and calculating models for a wider range of progenitor binaries. We have adopted the results of the SPH simulation into the 1D stellar evolution calculation and combined the resulting evolutionary tracks with the results of BSPS. We aim to compute the statistics and surface abundance of the post-merger systems, and compare these with observational data for Li-rich giants and early-R carbon stars. We aim to answer: When and how does a merger make lithium or carbon? How does the fresh material get to the surface? And how many Li-rich/early-R stars should be observed in the Galaxy?

In this paper, we define a Li-rich giant star as having $A(\mathrm{Li}) = \log_{10}(N(\mathrm{Li})/N(\mathrm{H})) + 12 > 1.5$ and a carbon star as having $N(\mathrm{C})/N(\mathrm{O}) > 1$ by numbers. In Section 2, we introduce the methods of constructing and evolving the models of post-mergers. The comparison of theory with observation of Li-rich giants and early-R stars is shown in Section 3. The discussion and conclusions are in Section 4.

2. Modeling the Mergers

Figure 1 shows a schematic sequence of events during an HeWD+RGB merger. Once the HeWD comes into contact with the expanding red giant, a common envelope (CE) forms. The HeWD will merge with the helium core of the giant if spiral-in occurs before the entire envelope is ejected. Then a single giant-like star forms that contains a hybrid core surrounded by a hydrogen-rich mantle. The structure of the hybrid core should be similar to the product of a double HeWDs merger, i.e., a degenerate core originating from the HeWD, surrounded by a very hot shell ($>10^8$ K) from the disrupted helium core of the progenitor red giant. Subsequently, the core will be heated by a series of He-burning shell flashes that burn inward toward the center. Finally, a red clump star forms once helium-core burning has been established.

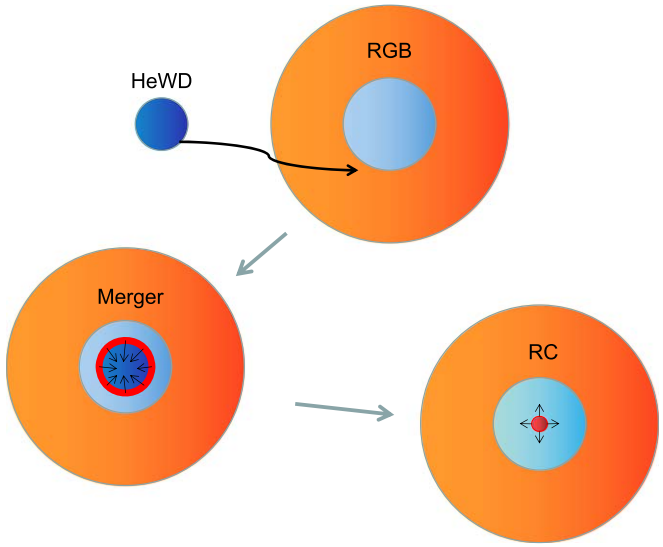

Figure 1. Schematic representation of possible steps in an HeWD plus RGB star merger leading to the formation of a red clump star with a lithium-rich or carbon-rich surface. Orange represents the hydrogen-rich envelope, blue is helium-rich material, and red represents the nuclear helium-burning region.

To represent such an evolutionary path in detail, three key steps are proposed in our model calculation. In step 1, information about potential merger progenitors is obtained from BSPS. In step 2, a grid of evolutionary tracks and surface abundances is calculated for an ensemble of post-merger models. In step 3, the characteristic properties of post-merger stars are calculated by combining the results of BSPS and the grid of post-merger evolutionary tracks.

2.1. Step 1: Binary Population Synthesis

To obtain details of the HeWD+RGB merger channel, we adopt BSPS to investigate whether the rate of possible mergers is sufficiently high to make a significant contribution to the population of Li-rich and C-rich giants. At same time, we calculate the masses of the HeWD and RGB progenitors that will be used for the subsequent calculation of post-merger evolution (Step 2).

We model populations of binary stellar stars with the BSE code (Hurley et al. 2000, 2002), starting from zero-age main-sequence (MS) stars. The basic parameters for binary-star evolution in the rapid evolution code in this work are chosen to be the same as those previously used to model the R stars by Izzard et al. (2007), which are also similar to those used by Politano et al. (2008, 2010). We evolve 10^7 pairs of stars within an evolution time of 14 Gyr and record the properties of HeWD +RGB binaries at the onset of the CE phase. The mass distribution of such pre-CE binaries will be used to set the grid of parameters for the calculations in steps 2 and 3.

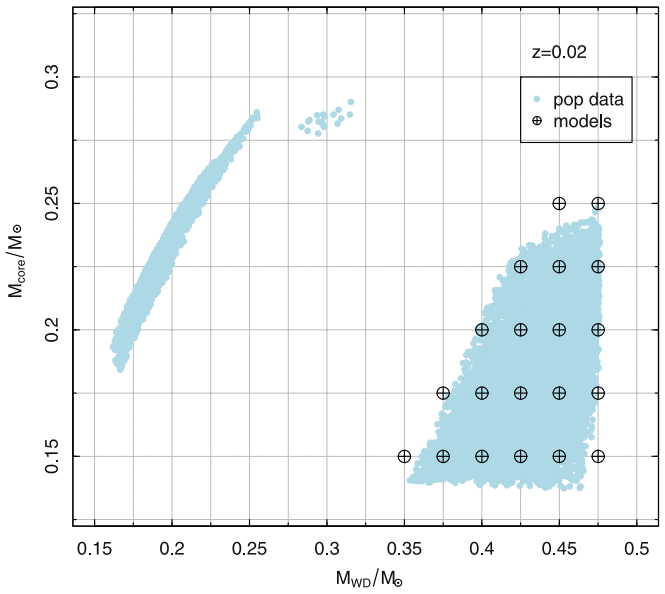

Figure 2. Models of HeWD+RGB merger remnants in the $M_{\rm WD}$+$M_{\rm core}$ plane. The circles with crosses indicate the merger models in this work. The dots indicate the masses of HeWD and core masses of the RGB stars in the pre-CE phase obtained in the binary population synthesis. The metallicity is $Z = 0.02$.

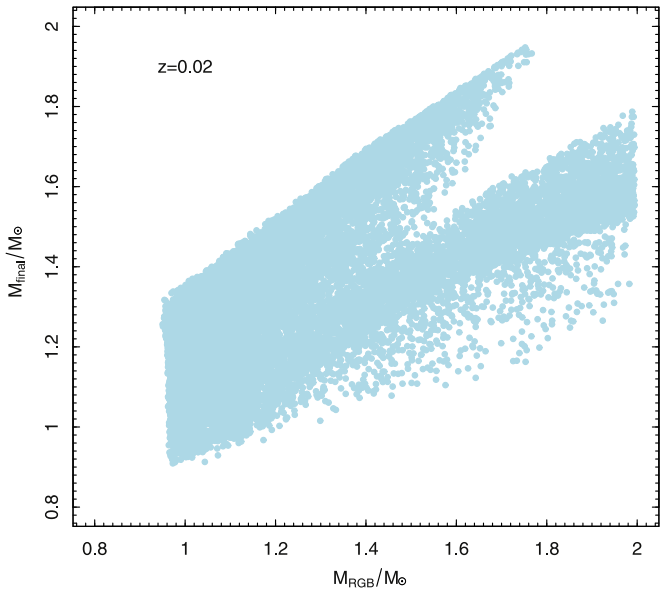

Figure 3. Initial and final masses of RGB stars in the pre-CE and post-merger phases. The metallicity is $Z = 0.02$.

We generate the mass ratio distribution of zero-age binary stars according to the formula of Eggleton et al. (1989) and adopt the initial mass function of Miller & Scalo (1979) in the range 0.08–100 $M_\odot$. The distribution of orbital separations, $p(a)$, is calculated by the formula of Han (1998):

$$p(a) = \begin{cases} 0.070(a/a_0)^{1.2} & a \leqslant a_0 \\ 0.070 & a_0 \leqslant a \leqslant a_1, \end{cases}$$

where $a_0 = 10\,R_\odot$, $a_1 = 5.75 \times 10^6\,R_\odot = 0.13$ pc. The parameters chosen in this work have been used in several previous studies on double WD mergers in the Galaxy (Han 1998; Zhang et al. 2014), hot subdwarfs (Han et al. 2002, 2003; Zhang & Jeffery 2012), SN Ia (Wang & Han 2009), and EL CVn stars (Chen et al. 2017).

Figure 2 shows the mass distribution of HeWDs and RGB cores with a metallicity of $Z = 0.02$ in the pre-CE phase. This is comparable with the results of Izzard et al. (2007). As in Izzard et al. (2007), the gap between the two populated regions is related to the initial periods of progenitor main-sequence binaries. The low-mass HeWDs form from short-period (few days) binaries and the high-mass HeWDs form from long-period (hundreds of days) binaries. The masses of the RGB star progenitors lie in the range 1–2 $M_\odot$, and will reduce after CE ejection. The final mass of the mergers shown in Figure 3 lies in the range 0.9–2 $M_\odot$.

2.2. Step 2: Post-merger Evolution

To examine features of the post-merger stars including the enrichment of elements, we used the stellar evolution code Modules for Experiments in Stellar Astrophysics (MESA) version V8118 (Paxton et al. 2011, 2013, 2015). To obtain the initial HeWDs, we evolved a 1.2 $M_\odot$ zero-age MS star until the He core reaches one of 0.350, 0.375, 0.400, 0.425, 0.450, or 0.475 $M_\odot$. Nucleosynthesis is switched off and a high mass-loss rate is applied to remove the hydrogen envelope completely, leaving a model of an exposed He core. Then the remnant core is allowed to cool to become a white dwarf, finally ending with a model having a surface luminosity $\log\,(L/L_\odot) = -2$ (Zhang & Jeffery 2012). According to Zhang & Jeffery (2013), surface enrichment following a merger only occurs for high-mass HeWDs. We also did a test for a low-mass HeWD merger model and confirmed such results. Hence, we have here chosen the masses of HeWDs to lie in the range 0.350–0.475 $M_\odot$ in steps of 0.025 $M_\odot$.

It is challenging to simulate a merger with a 1D stellar evolution code; however, a series of separate accretion steps is proposed to represent such a merger process and has previously been used successfully to represent some observations of merger remnants (Zhang & Jeffery 2012, 2013; Zhang et al. 2014, 2017). We separate the merger process into two accretion steps in this work, i.e., (1) accretion of helium-rich materials onto the HeWD to represent the process of the HeWD+RGB-core merger in the deep interior and then (2) accretion of hydrogen-rich materials to represent the assimilation of the surrounding RGB envelope by the new hot hybrid core. The fractional distribution of elements within the helium-rich material is computed from the average mass fractions of a 0.2 $M_\odot$ HeWD. The equivalent distribution within the hydrogen-rich material is computed from the average mass fraction of an envelope of a 1.2 $M_\odot$ RGB star. The accretion rate during the helium accretion phase is 10^{-3} $M_\odot$ yr^{-1}, which is similar to the average accretion rate obtained in the SPH simulation (Piersanti et al. 2010). An accretion rate of 1 $M_\odot$ yr^{-1} is used to re-establish the hydrogen-rich envelope around the merged core, as was used by Zhang et al. (2017). In all, the whole process takes place on a similar timescale to a CE phase (Ivanova 2011; Passy et al. 2012; Ivanova et al. 2013). The masses of the RGB helium cores range from 0.150 to 0.25 $M_\odot$ in steps of 0.05 $M_\odot$, as shown in Figure 2. In general, we set the initial hybrid-core masses of mergers to be the sum of masses of HeWD and RGB core, which will be modified by envelope convection during the merger process. The final masses of the merger combines contributions from the hybrid core and the envelope masses. The masses of final merged models range from 0.80 to 2.0 $M_\odot$ in

steps of 0.1 $M_\odot$ to cover the distribution of the final masses from a binary population synthesis of step 1 (see Figure 3). Thus, we obtained 259 initial models of post-merger stars for each metallicity, i.e., $Z = 0.03$, 0.02, 0.01, and 0.004.

For the subsequent post-merger evolution, we adopted parameters similar to the MESA Isochrones and Stellar Tracks (MIST) project for normal stars (Choi et al. 2016; Dotter 2016; see the Appendix). We set the mixing length parameter $\alpha = l/H_p = 1.82$. We adopt the OPAL Type 2 opacity tables in order to account for the changing abundances of carbon and oxygen following the He flashes (Iglesias & Rogers 1996; Ferguson et al. 2005). We chose the *simple photosphere* option for the outer boundary condition (i.e., $T^4(\tau) = 3/4\ T^4_{\rm eff}(\tau + 2/3)$). In our models, mixing is by convection in the convective regions and atomic diffusion in the radiative areas (Thoul et al. 1994). Diffusion includes the processes of gravitational settling, thermal diffusion, and concentration diffusion. The atomic diffusion coefficients are those calculated by Paquette et al. (1986). We also consider semiconvective and thermohaline mixing as in MIST. The mass-loss rate of the post-merger stars is computed according to Reimers's formula with $\eta_R = 0.5$. Nuclear reaction networks follow the abundances of 21 species: ^{1}H, ^{2}H, ^{3}He, ^{4}He, ^{7}Li, ^{7}Be, ^{8}B, ^{12}C, ^{13}C, ^{13}N, ^{14}N, ^{15}N, ^{16}O, ^{17}O, ^{18}O, ^{19}F, ^{22}Ne, ^{23}Na, ^{24}Mg, ^{27}Al, and ^{56}Fe.

2.3. Step 3: Population Synthesis of Post-mergers

We have the masses of progenitors from step 1 and a grid of evolutionary tracks of post-mergers from step 2. Hence, we can calculate the distribution of the post-merger models by combining both steps, from which we can obtain all the required parameters, i.e., the masses, surface effective temperature, surface gravity, and surface abundances. As shown in Figure 3 the final masses of the merged stars lie in a relatively small range. Thus, the evolutionary tracks are very close to each other for red giant evolution. But the variation of surface abundance is much more complex.

Therefore, we do not interpolate the paths for different masses, but instead we assume that stars with similar HeWDs, core masses, and final masses are on one of the theoretical evolutionary tracks that we have computed. We then calculate the number of merger remnants on each track from the BSPS prediction. We determine the evolutionary stage of each BSPS star along each track by a random sample selection that includes a probability weighted by the timescale associated with each point on the track.

3. Results

According to the CE merging process, the remnant contains a hybrid core with a hot helium shell ($>10^8$ K) surrounded by a hydrogen envelope. We adopt two separate fast-accretion phases to compute the structure of such a post-merger model. The surface abundance is enriched during the second (hydrogen) accretion phase.

Figure 4 shows the temperature structure of the hybrid core during the second accretion phase in the 0.40 $M_\odot$ HeWD + 0.15 $M_\odot$ helium-core RGB model. During the first ~10 steps of this phase, the convection zone can extend from the merged-star surface down to the hot helium shell. Hence, some material in the envelope can reach the hot layer (where the temperature $T > 10^7$ K) and therefore participate in nuclear reactions during this short interval. Hence, ^{3}He from the hydrogen envelope is

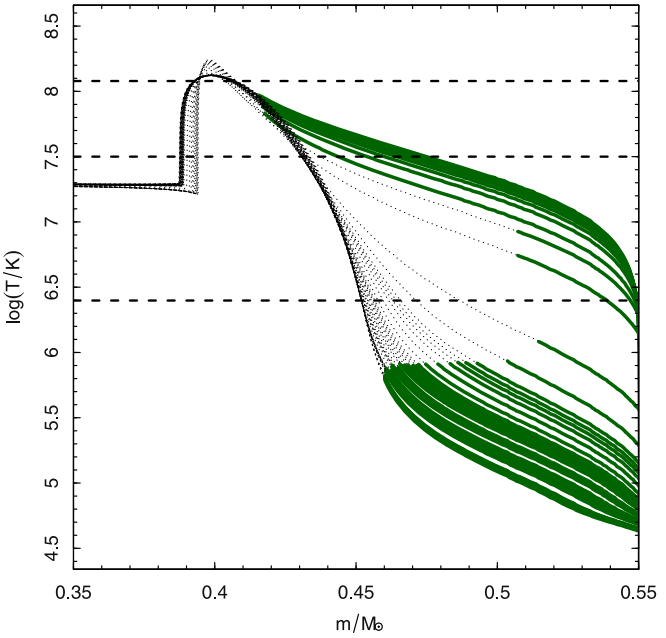

Figure 4. Temperature profile of a 0.40 $M_\odot$ HeWD + 0.15 $M_\odot$ helium-core RGB model, during the hydrogen-*assimilation* process. The dotted line shows the first 50 profiles of the model; the time increases from top to bottom. The thick (green) line indicates the convection-dominated region in each profile. Three dashed lines indicate the *approximate minimum* temperatures for the 3α reaction ($T = 1.2 \times 10^8$ K; e.g., Suda et al. 2011), Cameron–Fowler mechanism reaction ($T = 3 \times 10^7$ K; e.g., Sackmann & Boothroyd 1992), and lithium destruction ($T = 2.5 \times 10^6$ K; e.g.,Pinsonneault 1997), respectively. During the interval shown here, the mass of the hydrogen envelope (not shown) increases from 0 to 0.02 $M_\odot$.

mixed with ^{4}He in the hot helium shell and produces the fresh ^{7}Li by the ^{3}He(α, γ)^{7}Be(e^-, ν)^{7}Li reaction once $T > 3 \times 10^7$ K. Meanwhile, fresh ^{7}Li will be destroyed by the ^{7}Li(p, α)^{4}He reaction regions where $T > 2.5 \times 10^6$. The convection zone will shrink away from the hot shell and back to a region where the temperature is less than 2.5×10^6 after the first ~20 steps. Thus, we expect some newborn ^{7}Li to survive. The final abundance of ^{7}Li depends on the creation and destruction processes in the hot shell. In our merger models, there is no new carbon carried to the surface because the convection zone does not reach the region of 3α burning that requires $T > 1.2 \times 10^8$ (Suda et al. 2011).

As in the HeWD+HeWD merger, the temperature of hot shells depends on the masses of the HeWDs (Zhang & Jeffery 2012; Zhu et al. 2013; Dan et al. 2014). Thus, a more massive HeWD will form a hotter and broader helium-burning shell during the merger process. Because of the higher temperature, less ^{7}Li will survive, but carbon from 3α burning will be elevated to the surface by convection.

For the intermediate-mass HeWDs, the surface convection zone does not contact the helium-burning region, but still reaches a layer where it is hot enough to destroy almost all fresh ^{7}Li. Figure 5 shows that the remnants of the merger are divided into three groups, i.e., Li-rich giants, C-rich giants, and normal stars, which depend on the HeWD progenitor masses. Hence, we will discuss the mass ranges for these different cases separately.

3.1. Li-rich Red Clump Stars

As discussed above, only the post-merger models formed from less massive HeWDs can produce models with Li-rich

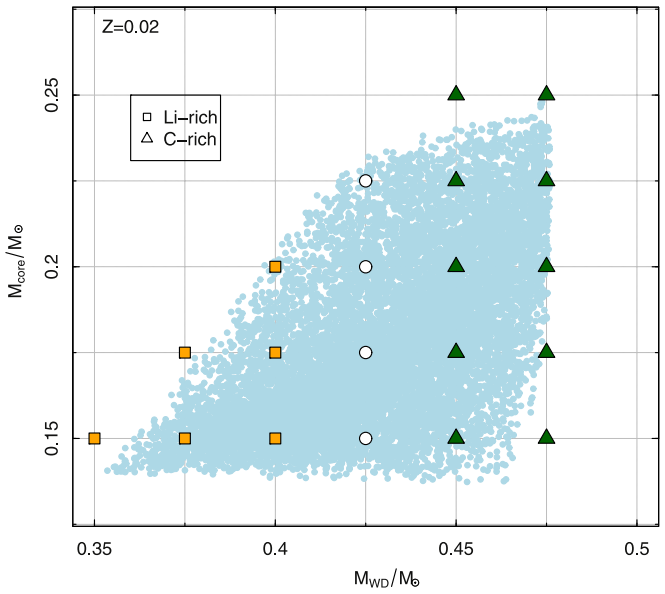

Figure 5. Similar to Figure 2, models of merged HeWD+RGB remnants in the M_{WD}–M_{core} plane. The squares (orange) indicate Li-rich merged models, and the triangles (green) show C-rich merged models. The circles indicate unenriched models. The metallicity is $Z = 0.02$.

surfaces, i.e., HeWD models with masses of 0.35, 0.375, and 0.40 $M_\odot$ in our calculations. As shown in Figure 6, the radius of the star decreases during the inward helium flash before core burning. The inward helium-core-shell burning takes about 3 Myr. Then the helium-burning flame turns outward and to stars in red clump stages. The abundance of lithium decreased during the core-burning phase, which takes tens of million years (see Figure 7). Once core-helium-burning ceases, stars evolve to the AGB phase.

Considering that our post-merger models spend most of their Li-rich stage in the helium-core-burning phase, we expect to observe the majority as red clump stars. Most of the Li-rich giants are close to the location of the red clump on either the HR diagram or $T_{\rm eff}$–log g plane (e.g., Kumar et al. 2011; Adamów et al. 2014; Casey et al. 2016; Deepak & Reddy 2019; Singh et al. 2019a; Zhou et al. 2019). However, it is difficult to distinguish whether an observed giant is a red clump giant or is a degenerate-core giant ascending the RGB for the first time (a red bump giant) from their external parameters alone, i.e., from their luminosity, gravity, and temperature. The best way to distinguish between these two stages is by asteroseismology (Bedding et al. 2011). About 30 Li-rich stars have been examined by these means (e.g., Carlberg et al. 2015; Jofré et al. 2015; Bharat Kumar et al. 2018; Singh et al. 2019b, 2019a). Having found that model HeWD+RGB merger remnants can become Li-rich red giants, we compare their properties with observed examples in more detail.

3.1.1. Luminosity, Effective Temperature, and Surface Gravity

We compile a sample of 439 observed Li-rich giants for which parameters of luminosity, surface effective temperature, and gravity have been published (Kumar et al. 2011; Carlberg et al. 2015; Jofré et al. 2015; Bharat Kumar et al. 2018; Deepak & Reddy 2019; Singh et al. 2019a, 2019b; Zhou et al. 2019). Of these, the evolution stage has been determined for 30. All

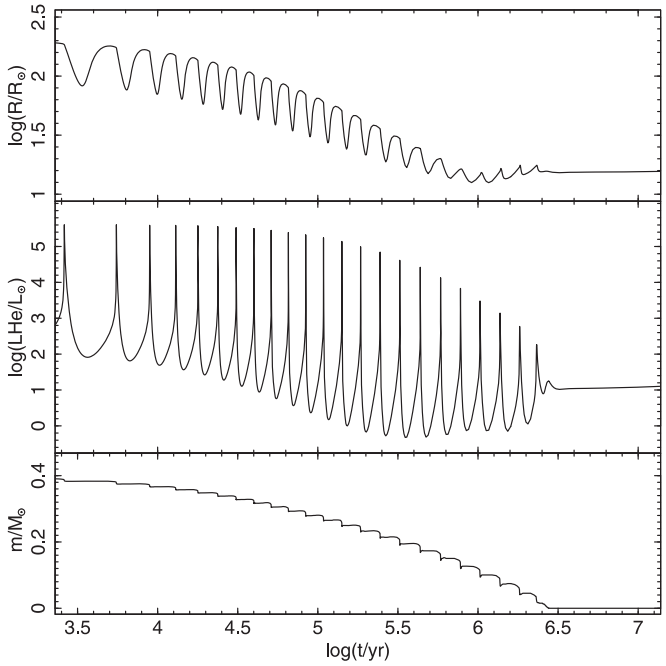

Figure 6. Post-merger evolution of a 0.40 $M_\odot$ HeWD+0.15 $M_\odot$ helium-core RGB with a final mass of 1.10 $M_\odot$ before core burning. Top panel: the evolution of radius. Middle panel: energy generated from the 3α reaction. Bottom panel: the location of helium-burning flame front.

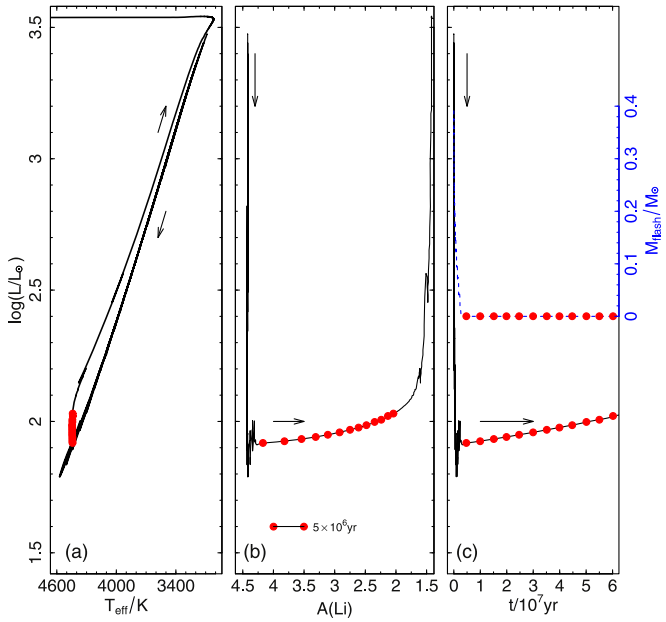

Figure 7. Evolutionary tracks of the same model as in Figure 6. Left panel: evolution in the HR diagram. Middle panel: the evolution of surface abundance of lithium. Right panel: the evolution of luminosity and helium flash location (dotted line, right-hand axis) as a function of time. Red dots are separated in time by 5×10^6 yr.

30 are red clump stars (Carlberg et al. 2015; Jofré et al. 2015; Bharat Kumar et al. 2018; Singh et al. 2019a, 2019b). In the log g–$T_{\rm eff}$ plane, their locations are similar to the theoretical loci of Li-rich giants formed through HeWD+RGB mergers (Figure 8). The 30 known Li-rich red clump stars match the peak of the theoretical distribution very well. A similar

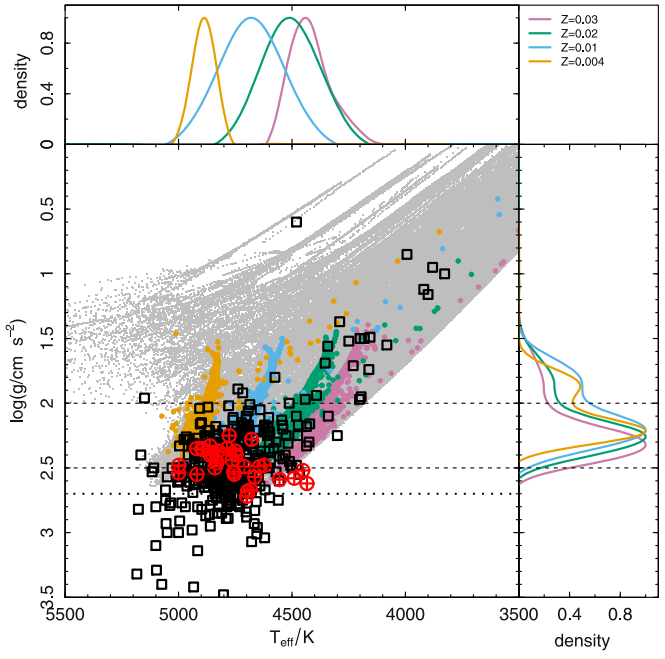

Figure 8. Lithium-rich giants in the effective temperature–surface gravity plane. The gray dots indicate all the theoretical HeWD+RGB merger tracks computed that produce Li-rich giants. The colored dots show the possible locations of Li-rich models from BSPS, with different colors for different metallicity Z as labeled in the key (top right). The squares represent observed Li-rich giants without asteroseismology. The 30 known Li-rich red clump stars are shown as circles with crosses. The dashed lines delimit the most likely range (in log g) for Li-rich giants from BSPS. The dotted line marks the maximum gravity of our Li-rich models. In the top left and lower right panels, curves color coded for metallicity represent the normalized number density distributions of the Li-rich BSPS models in $T_{\rm eff}$ and log g, respectively.

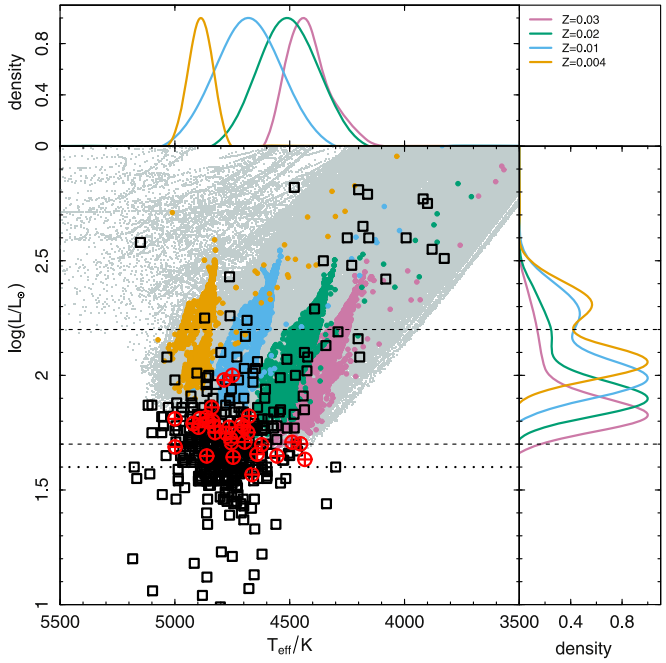

Figure 9. As Figure 8, but for the L–$T_{\rm eff}$ plane (HR diagram).

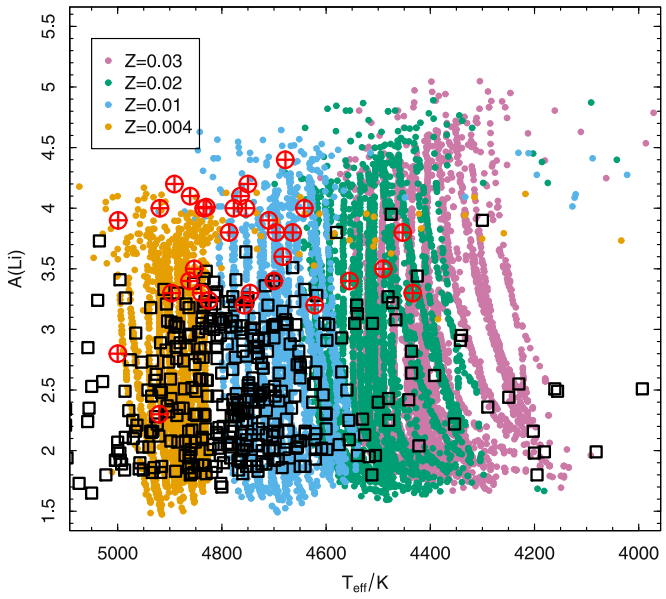

Figure 10. Observed Li-rich giants in the effective temperature–surface lithium (A(Li)) plane. Symbols are as in Figure 8.

comparison can be made in the L–$T_{\rm eff}$ plane (HR diagram: Figure 9).

3.1.2. Surface Abundance

The most important feature to compare with observation is the abundance of lithium. Figure 10 shows the lithium distribution of observation stars on the A(Li)–T plane, and almost all can be represented by our models.

In addition to the abundance of the lithium, carbon isotope ratios are known for a few Li-rich giants, most of which show a low $^{12}C/^{13}C$ ratio (<15) (Kumar et al. 2011). We compiled a sample of 39 Li-rich giants with a known $^{12}C/^{13}C$ ratio to compare with our models (Figure 11). Most of the observed ratios match the theoretical distribution of $^{12}C/^{13}C$ in Li-rich giant models. The enrichment of ^{13}C is due to the $^{12}C(p, \gamma)^{13}N(\beta^+, \nu)^{13}C(p, \gamma)^{14}N$ reaction followed by convective mixing (or dredge-up) to the surface during the merger. The final fraction of ^{13}C depends on the balance of the competition of ^{13}C and ^{14}N in the nuclear reactions.

3.1.3. Red Clump Status

As stated above, the post-merger models spend several million years with a helium-burning shell moving inward though a helium core. Once the helium flash front reaches the center, actual core-helium-burning begins. They then spend most of their lifetime as red giants in the red clump stage, i.e., tens of millions of years. We would therefore expect most Li-rich giants to be red clump stars if they are formed by a merger. As shown in Figure 12, the helium-core-burning stars (red clump stars) and hydrogen-shell-burning stars (RGB stars) occupy different regions of the $\Delta\nu$–Δp diagram.[4] The red clump stars typically have $\Delta\nu/\mu{\rm Hz} \sim 5$ and $200 < \Delta p/{\rm s} < 400$. The RGB stars typcially have $\Delta p/{\rm s} \sim 100$ and $4 < \Delta\nu/\mu{\rm Hz} < 20$. In other words, the red clump stars demonstrate a large range of core properties, while the RGB stars demonstrate a large range of envelope properties. All 30 Li-rich giants are red clump stars, and most match those theoretical models allowed by BSPS.

[4] $\Delta\nu$ and Δp represent the large frequency and large period spacing that, in asymptotic theory, are characteristic of the spacing between successive radial orders of p- and g-mode oscillations of the same (nonradial) degree that, in turn, primarily reflect properties of the stellar envelope and core, respectively.

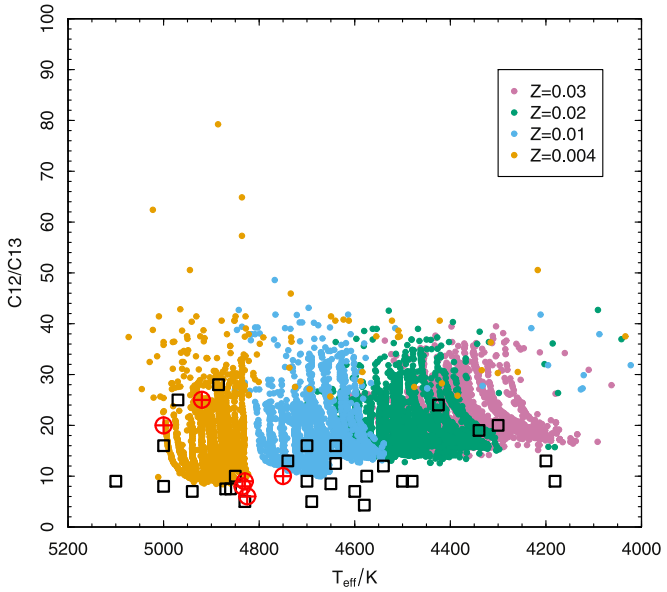

Figure 11. Observed Li-rich giants in the effective temperature–surface $^{12}C/^{13}C$ plane. Symbols are as in Figure 8.

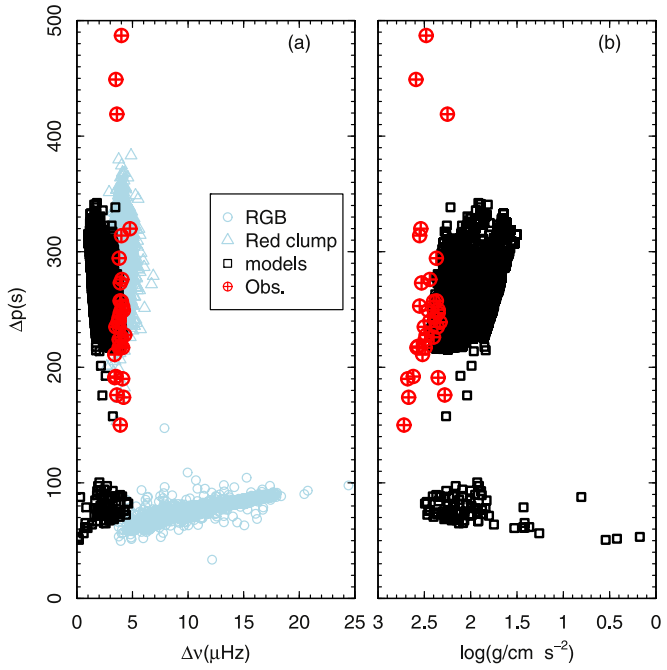

Figure 12. Location of the sample stars and models on the seismic diagram (left) and log g–Δp plane (right). The red clump stars and RGB stars are indicated by triangles and circles, which are from Vrard et al. (2016). The squares and circles with crosses indicate the models and observed Li-rich giants, respectively.

The same stars and models are shown on the log g–Δp plane (also Figure 12) and also match well. We calculate the asteroseismic quantities from simple scaling relations (e.g., Ulrich 1986; Brown et al. 1991; Kjeldsen & Bedding 1995) using MESA output, and not from a full pulsation analysis (Townsend & Teitler 2013, e.g., GYRE). The former are used successfully for asteroseismic analyses of many classes of pulsating star.

Figure 12 shows that there are a few post-merger models in the RGB-dominated region of the seismic diagram. Such models are in the helium-core-shell-burning phase, where the helium-burning

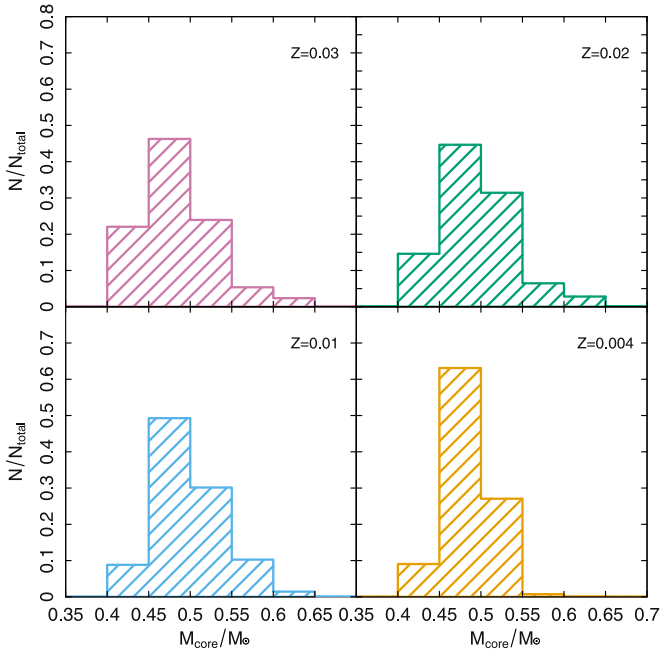

Figure 13. Core mass distribution of Li-rich giant models at different metallicities.

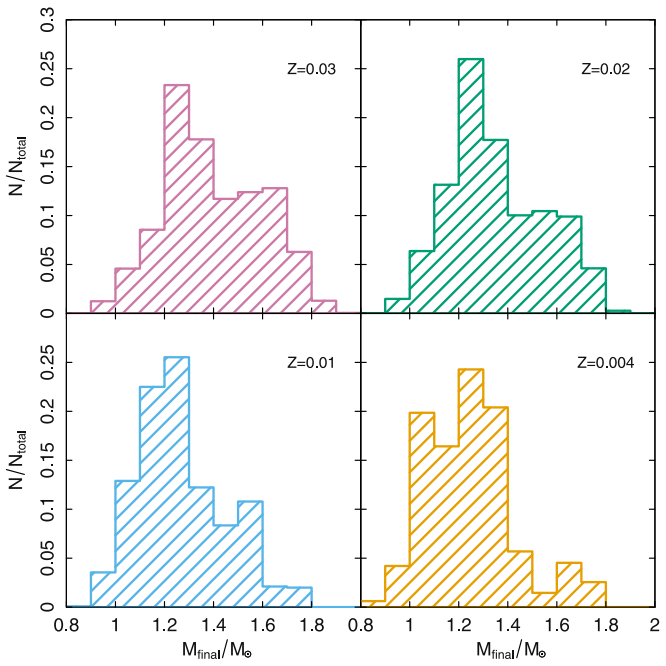

Figure 14. Total mass distribution of Li-rich giant models at different metallicities.

shell is moving inward into an electron-degenerate helium core. Their density structure is thus similar to that of RGB stars where the hydrogen-burning shell around an election-degenerate helium core is moving outward.

3.1.4. Masses

Figure 13 shows the distribution of the core masses of merger remnants. The core masses are in the range 0.4−0.65 $M_{\odot}$, with a peak at 0.45−0.5 $M_{\odot}$. Figure 14 shows the final masses of

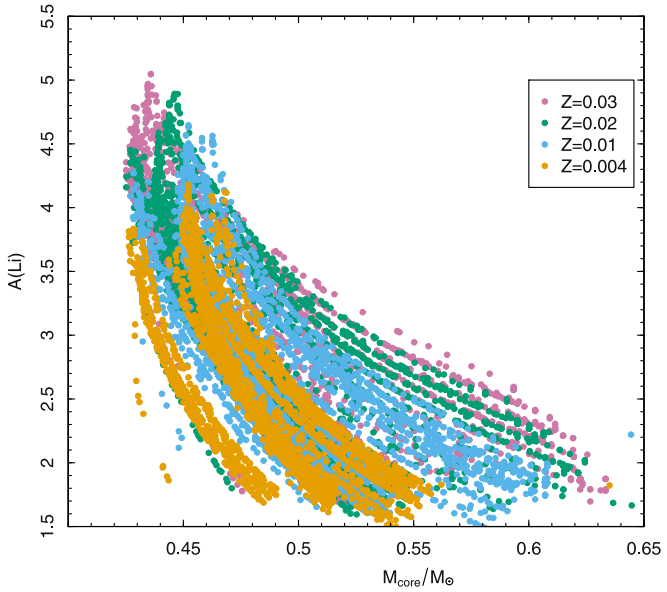

Figure 15. Core mass–*A*(Li) plane. Symbols are as in Figure 8.

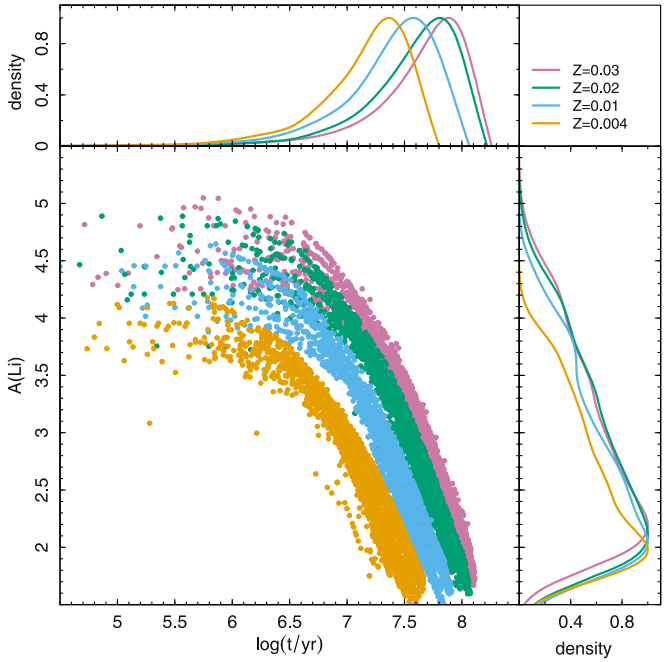

Figure 16. Surface lithium abundances of Li-rich models as a function of age. Symbols are as in Figure 8.

Li-rich mergers, which range from 0.8 to 1.8 $M_{\odot}$. The peak of the mass distribution is ≈1.2 $M_{\odot}$.

As discussed in Section 2, the abundance of lithium in the post-merger models is very sensitive to the mass of the pre-merger HeWDs and hence to the core masses of the remnants. Figure 15 shows how the surface abundance of lithium increases with decreasing core mass. For stars with lithium *A* (Li) $\geqslant$ 3.2, the core masses are approximately in the range 0.44 −0.51 $M_{\odot}$.

3.1.5. Birth Rate

Aside from the question of how lithium is enriched by HeWD+RGB mergers, a critical issue is how many such stars could be observed in the Galaxy. To find the answer, we combine post-merger evolution models with the results of population synthesis and a statistical analysis. Our calculation is designed to find the properties of a model population with an age of 14 Gyr and a constant star formation rate of 5 $M_{\odot}$ yr^{-1}, which is designed to represent star formation history of the Galaxy (Yungelson & Livio 1998).

From a calculation of 10^7 binary systems, we find that 3931, 3233, 2707, and 3093 undergo HeWD+RGB mergers and produce enriched lithium surfaces for metallicities $Z = 0.03$, 0.02, 0.01, and 0.004, respectively. Thus, at an age of 13.7 Gyr with a constant star formation rate of 5 $M_{\odot}$ yr^{-1}, Li-rich giants form through HeWD+RGB mergers at a rate of 8.6, 7.0, 5.9, and 6.7 $\times$ 10^{-4} yr^{-1} for the Galaxy disk at $Z = 0.03$, 0.02, 0.01, and 0.004, respectively.

Another factor to consider is the lifetime of Li-rich giants. Lithium will decrease during evolution as surface lithium is dredged down and destroyed. Figure 16 shows the ages of Li-rich giants in our models since the post-merger stage. The most enriched lithium giants only exist as such for a few millions of years, but in total, the Li-rich giants defined as having *A* (Li) > 1.5 may live for up to 1.0 $\times$ 10^8 yr. Assuming a birth rate of (6−9) $\times$ 10^{-4} yr^{-1} and taking an effective Galactic disk volume of 7.5 $\times$ 10^{10} pc^3 (e.g., Yu & Jeffery 2015) we expect the Galactic disk volume density of Li-rich giants to be (0.8−1.2) $\times$ 10^{-6} pc^{-3}, assuming that the majority are Li-rich red clump stars. The apparent space density of red clump stars is about 1.14 $\times$ 10^{-4} pc^{-3} in the disk of the Galaxy (Knapp et al. 2001). The predicted number of Li-rich red clump stars formed from mergers thus corresponds to ∼1% of the total red clump stars. This suggests that HeWD+RGB mergers contribute to most of the observed Li-rich red clump population. However, some Li-rich giants may form from other channels, in particular the Li-rich red bump RGB stars.

3.2. Early-R Carbon Stars

Zhang & Jeffery (2013) argued that the early-R carbon stars could form from HeWD+RGB mergers. In the current merger calculations we can reproduce the features of most early-R carbon stars. As with Li-rich stars from the HeWD+RGB merger channel, the models that resemble early-R stars are all in the red clump (core-helium-burning) phase, but with the difference that these models are formed from more massive HeWDs. Moreover, we only obtain carbon-rich models with metallicities $Z = 0.03$, 0.02, and 0.01, and *not* with $Z = 0.004$.

Having found that model HeWD+RGB merger remnants can become early-R stars, we compare their properties in more detail to observed examples of such stars. We have a sample of 12 early-R stars from Zamora et al. (2009). We compare these stars with the theoretical distribution of atmospheric parameters for models formed through this merger channel. The observed stars are satisfactorily close to the theoretical distribution in the effective temperature–surface gravity plane (Figure 17).

3.2.1. General Properties

Figure 18 compares the C/O and ^{12}C/^{13}C ratios for the early-R star observations with ratios calculated in the models. The theoretical models overlap the distribution of early-R stars with C/O ≈ 1−2. Some of the stars with large C/O ratio may form from other channels. The observed lithium abundances are shown in Figure 19 and are consistent with the range obtained in the

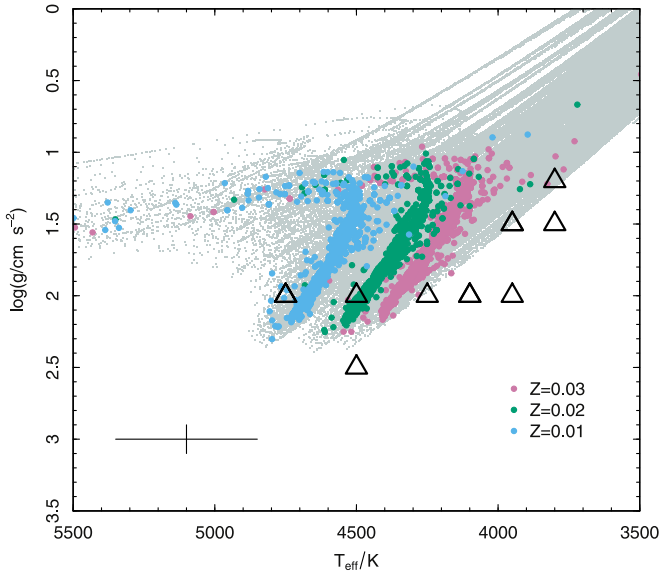

Figure 17. Early-R stars in the effective temperature–surface gravity plane. The gray dots indicate the theoretical distribution of C-rich models formed through HeWD+RGB mergers. The colored dots show the possible location of stars from binary population synthesis, with different colors for different metallicities. The triangles represent observed early-R stars from Zamora et al. (2009). The cross indicates the average error on the R-star observations.

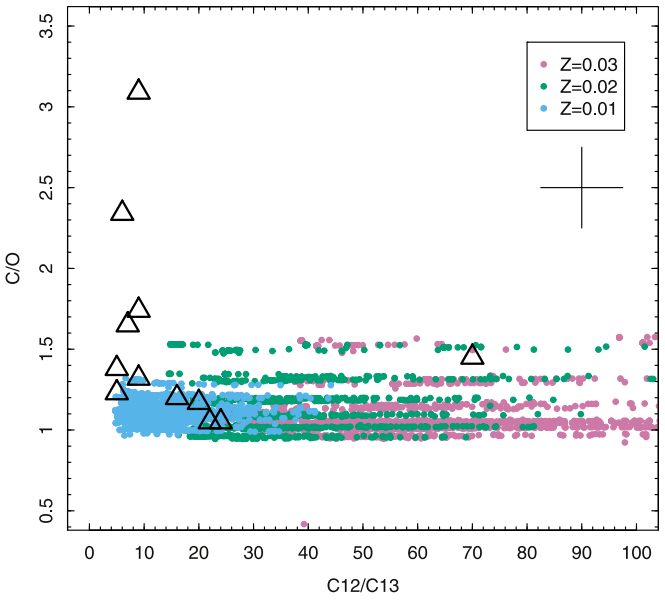

Figure 18. As in Figure 17, but for C/O and $^{12}C/^{13}C$ ratios.

merger models. The observed $^{12}C/^{13}C$ ratios are consistent with models having $Z \sim 0.01$. Of the 12 stars, 8 have [M/H] <= −0.3 ($Z \sim 0.01$) and the rest are −0.26, −0.1,−0.09, and −0.03 (Zamora et al. 2009). Thus, a metal-poor origin appears probable.

3.2.2. Birth Rate

As in the study of Li-rich giants, we want to know how many early-R stars formed from merger we can expect to observe in the Galaxy. From the BSPS simulation of 10^7 binary systems, we find 2051, 1262, and 1742 systems that undergo HeWD+RGB mergers to produce enriched carbon stars, with $Z = 0.03$, 0.02, and 0.01, respectively. Thus, at 13.7 Gyr, with a constant star

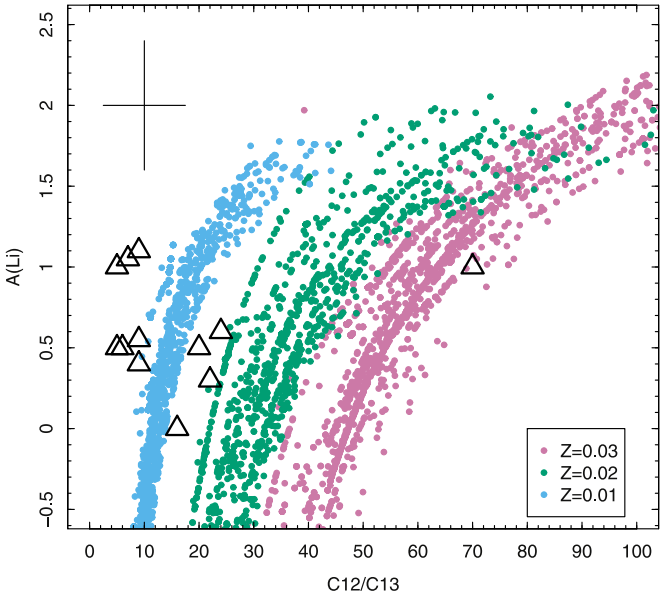

Figure 19. As in Figure 17, but for A(Li) and $^{12}C/^{13}C$.

formation rate of 5 $M_\odot$ yr^{-1}, C-rich giants are formed through HeWD+RGB mergers at a rate of 4.4, 2.6, and 3.8 × 10^{-4} yr^{-1} for the Galaxy disk at $Z = 0.03$, 0.02, and 0.01, respectively.

The lifetime for C-rich giants is about 10^8 yr. Combined with the birth rate and the volume of the disk of Galaxy, we may expect the volume density of early-R stars to be (3.5−5.9) × 10^{-7} pc^{-3}. The observed volume density of early-R stars is about (0.45 − 1.5) × 10^{-7} pc^{-3} (Knapp et al. 2001). These are small number statistics, but they do indicate that HeWD+RGB mergers can contribute for the early-R star populations. Other channels may account for the most carbon-rich early-R stars.

4. Conclusion and Discussion

The merger of an HeWD with an RGB star in a CE provides a possible model for the origin of lithium- and carbon-rich stars. By adopting a grid of approximate initial conditions for such mergers informed by previous SPH simulations, we have made one-dimensional MESA calculations of the post-merger evolution of a wide range of possible systems. Using BSPS we have computed the frequency and distribution of HeWD + RGB binary-star systems that are likely to merge.

Analysis of the post-merger evolution models show that the final surface abundances depend on the masses of the progenitor HeWDs. The Li-rich giants form from low-mass HeWDs, i.e., $0.35\,M_\odot \leqslant M_{\rm WD} \leqslant 0.40M_\odot$; the C-rich giants form from low-mass HeWDs, i.e., $0.45\,M_\odot \leqslant M_{\rm WD} \leqslant 0.475M_\odot$. The pathway to either of these categories is related to the temperature of the helium-core-burning shell and the balance of nuclear products during initial shell burning.

Analysis of the distribution of post-merger systems, as given by BSPS and MESA evolution tracks, shows that predictions for HeWD+RGB mergers are consistent with observations of most Li-rich giants in terms of surface effective temperature ($T_{\rm eff}$), surface gravity (log g), surface luminosity (log L), surface abundance (A(Li) and $^{12}C/^{13}C$), and the Galaxy disk space density of (0.8 − 1.2) × 10^{-6} pc^{-3}. They are also consistent with the properties of some early-R carbon stars, in terms of $T_{\rm eff}$, log g, C/O, A(Li), $^{12}C/^{13}C$, and a space density of (3.5−5.9) × 10^{-7} pc^{-3}.

According to the models, the post-merger objects are helium-core-burning stars, which means that they are all in the red clump stage of evolution, i.e., they are red giants with nondegenerate helium cores. However, only a few Li-rich giants have had their precise evolutionary stage determined by asteroseismology. Those stars that have been analyzed in this way correspond well with our results. Hence, we strongly argue that the Li-rich red clump stars and the majority of early-R carbon stars most likely form following the merger of an HeWD with an RGB star.

A few problems still need to be addressed:

(i) Post-merger evolution calculations depend on evolution during the CE phase that is determined by the progenitors of the merger, the amount of mass loss during the CE phase, and the structure of the CE. However, our knowledge of CE phase in binary-star evolution is still poor. Future theoretical studies and simulations will improve this deficiency. Also, as the products of post-CE mergers, further observations of Li-rich red clump stars will provide additional data for studies of the CE phase.

(ii) Some of the observed Li-rich giants have measured rotation velocities, but we have not calculated rotation speeds for post-merger models immediately following CE ejection. Our model will be improved with more knowledge of angular momentum transport during the merger.

(iii) The HeWD+RGB merger model provides a successful explanation for Li-rich red clump stars, but does not explain Li-rich RGB stars, i.e., stars on their first ascent of the giant branch. Such stars will require further explanation in the future.

(iv) The most carbon-rich early-R stars (with $C/O \gg 1.5$) cannot be explained by our models.

We therefore need more observations of Li-rich and C-rich giants to help identify and diagnose the evolution channels. We also require further numerical simulations for HeWD+RGB mergers, in particular to study the dynamics of the CE and the merging of the HeWD with the RGB core.

We would like to thank the referee for the helpful suggestions and comments that improved the manuscript. X.Z. thanks Hongliang Yan, Haining Li, and Yerra Bharat Kumar for helpful conversations. This work is supported by the grants 11703001, 10933002, and 11273007 from the National Natural Science Foundation of China, the Joint Research Fund in Astronomy (U1631236) under cooperative agreement between the National Natural Science Foundation of China (NSFC) and Chinese Academy of Sciences (CAS), and the Fundamental Research Funds for the Central Universities. Armagh Observatory and Planetarium is supported by a grant from the Northern Ireland Department for Communities.

Appendix
MESA Inlist

To evolve merger remnants with MESA the parameters that differ from the defaults are as follows:

```
&star_job
 change_net = .true.
 new_net_name = 'agbnew.net'
 set_rates_preference = .true.
 new_rates_preference = +2
 kappa_file_prefix = 'a09'
 kappa_lowT_prefix = 'lowT_fa05_a09p'
 kappa_CO_prefix = 'a09_co'
 initial_zfracs = 6 ! AGSS09_zfracs
/
&controls
 use_Type2_opacities = .true.
 kap_Type2_full_off_X = 1d-3
 kap_Type2_full_on_X = 1d-6
 Zbase = 0.02d0
 mixing_length_alpha = 1.82
 use_Ledoux_criterion = .true.
 alpha_semiconvection = 0.1
 thermohaline_coeff = 666.0
 which_atm_option = 'simple_photosphere'
 cool_wind_RGB_scheme = 'Reimers'
 Reimers_scaling_factor = 0.5
 cool_wind_AGB_scheme = 'Blocker'
 Blocker_scaling_factor = 0.5
 RGB_to_AGB_wind_switch = 1d-4
 varcontrol_target = 1d-3
 mesh_delta_coeff = 2
 do_element_diffusion = .true.
 diffusion_dt_limit = 3.15e13
 diffusion_min_T_at_surface = 1d3
```


ORCID iDs

Xianfei Zhang https://orcid.org/0000-0002-3672-2166
C. Simon Jeffery https://orcid.org/0000-0003-1759-0302
Shaolan Bi https://orcid.org/0000-0002-7642-7583

References

Abia, C., & Isern, J. 2000, ApJ, 536, 438
Adamów, M., Niedzielski, A., Villaver, E., Wolszczan, A., & Nowak, G. 2014, A&A, 569, A55
Aguilera-Gómez, C., Chanamé, J., Pinsonneault, M. H., & Carlberg, J. K. 2016, ApJL, 833, L24
Ashwell, J. F., Jeffries, R. D., Smalley, B., et al. 2005, MNRAS, 363, L81
Bedding, T. R., Mosser, B., Huber, D., et al. 2011, Natur, 471, 608
Bharat Kumar, Y., Singh, R., Eswar Reddy, B., & Zhao, G. 2018, ApJL, 858, L22
Brown, J. A., Sneden, C., Lambert, D. L., & Dutchover Edward, J. 1989, ApJS, 71, 293
Brown, T. M., Gilliland, R. L., Noyes, R. W., & Ramsey, L. W. 1991, ApJ, 368, 599
Cameron, A. G. W., & Fowler, W. A. 1971, ApJ, 164, 111
Carlberg, J. K., Smith, V. V., Cunha, K., et al. 2015, ApJ, 802, 7
Casey, A. R., Ruchti, G., Masseron, T., et al. 2016, MNRAS, 461, 3336
Charbonnel, C., & Balachandran, S. C. 2000, A&A, 359, 563
Chen, X., Maxted, P. F. L., Li, J., & Han, Z. 2017, MNRAS, 467, 1874
Choi, J., Dotter, A., Conroy, C., et al. 2016, ApJ, 823, 102
Dan, M., Rosswog, S., Brüggen, M., & Podsiadlowski, P. 2014, MNRAS, 483, 14
Deepak, & Reddy, B. E. 2019, MNRAS, 484, 2000
Denissenkov, P. A., & Herwig, F. 2004, ApJ, 612, 1081
Dominy, J. F. 1984, ApJS, 55, 27
Dotter, A. 2016, ApJS, 222, 8
Eggleton, P. P., Fitchett, M. J., & Tout, C. A. 1989, ApJ, 347, 998
Ferguson, J. W., Alexander, D. R., Allard, F., et al. 2005, ApJ, 623, 585
Fleming, W., & Pickering, E. C. 1908, HarCi, 145, 1
Han, Z. 1998, MNRAS, 296, 1019
Han, Z., Podsiadlowski, P., Maxted, P. F. L., & Marsh, T. R. 2003, MNRAS, 341, 669
Han, Z., Podsiadlowski, P., Maxted, P. F. L., Marsh, T. R., & Ivanova, N. 2002, MNRAS, 336, 449
Hurley, J. R., Pols, O. R., & Tout, C. A. 2000, MNRAS, 315, 543
Hurley, J. R., Tout, C. A., & Pols, O. R. 2002, MNRAS, 329, 897
Iben, I. J. 1967a, ApJ, 147, 650
Iben, I. J. 1967b, ApJ, 147, 624

Iglesias, C. A., & Rogers, F. J. 1996, ApJ, 464, 943
Ivanova, N. 2011, in ASP Conf. Ser. 447, Evolution of Compact Binaries, ed. L. Schmidtobreick, M. R. Schreiber, & C. Tappert (San Francisco: ASP), 91
Ivanova, N., Justham, S., Avendano Nandez, J. L., & Lombardi, J. C. 2013, Sci, 339, 433
Izzard, R. G., Jeffery, C. S., & Lattanzio, J. 2007, A&A, 470, 661
Jofré, E., Petrucci, R., García, L., & Gómez, M. 2015, A&A, 584, L3
José, J., & Hernanz, M. 1998, ApJ, 494, 680
Kjeldsen, H., & Bedding, T. R. 1995, A&A, 293, 87
Knapp, G., Pourbaix, D., & Jorissen, A. 2001, A&A, 371, 222
Kumar, Y. B., Reddy, B. E., & Lambert, D. L. 2011, ApJL, 730, L12
Li, H., Aoki, W., Matsuno, T., et al. 2018, ApJL, 852, L31
Lind, K., Primas, F., Charbonnel, C., Grundahl, F., & Asplund, M. 2009, A&A, 503, 545
Miller, G. E., & Scalo, J. M. 1979, ApJS, 41, 513
Paquette, C., Pelletier, C., Fontaine, G., & Michaud, G. 1986, ApJS, 61, 177
Passy, J.-C., De Marco, O., Fryer, C. L., et al. 2012, ApJ, 744, 52
Paxton, B., Bildsten, L., Dotter, A., et al. 2011, ApJS, 192, 3
Paxton, B., Cantiello, M., Arras, P., et al. 2013, ApJS, 208, 4
Paxton, B., Marchant, P., Schwab, J., et al. 2015, ApJS, 220, 15
Piersanti, L., Cabezón, R. M., Zamora, O., et al. 2010, A&A, 522, A80
Pinsonneault, M. 1997, ARA&A, 35, 557
Politano, M., Taam, R. E., van der Sluys, M., & Willems, B. 2008, ApJL, 687, L99
Politano, M., van der Sluys, M., Taam, R. E., & Willems, B. 2010, ApJ, 720, 1752
Sackmann, I. J., & Boothroyd, A. I. 1992, ApJL, 392, L71
Sackmann, I. J., & Boothroyd, A. I. 1999, ApJ, 510, 217
Secchi, A. 1868, MNRAS, 28, 196
Sengupta, S., Izzard, R. G., & Lau, H. H. B. 2013, A&A, 559, A66
Singh, R., Reddy, B. E., Bharat Kumar, Y., & Antia, H. M. 2019a, ApJL, 878, L21
Singh, R., Reddy, B. E., & Kumar, Y. B. 2019b, MNRAS, 482, 3822
Suda, T., Hirschi, R., & Fujimoto, M. Y. 2011, ApJ, 741, 61
Thoul, A. A., Bahcall, J. N., & Loeb, A. 1994, ApJ, 421, 828
Townsend, R. H. D., & Teitler, S. A. 2013, MNRAS, 435, 3406
Ulrich, R. K. 1986, ApJL, 306, L37
Vrard, M., Mosser, B., & Samadi, R. 2016, A&A, 588, A87
Wang, B., & Han, Z. 2009, A&A, 508, L27
Yan, H.-L., Shi, J.-R., Zhou, Y.-T., et al. 2018, NatAs, 2, 790
Yu, S., & Jeffery, C. S. 2015, MNRAS, 448, 1078
Yungelson, L., & Livio, M. 1998, ApJ, 497, 168
Zamora, O., Abia, C., Plez, B., Domínguez, I., & Cristallo, S. 2009, A&A, 508, 909
Zhang, X., Hall, P. D., Jeffery, C. S., & Bi, S. 2017, ApJ, 835, 242
Zhang, X., & Jeffery, C. S. 2012, MNRAS, 419, 452
Zhang, X., & Jeffery, C. S. 2013, MNRAS, 430, 2113
Zhang, X., Jeffery, C. S., Chen, X., & Han, Z. 2014, MNRAS, 445, 660
Zhou, Y., Yan, H., Shi, J., et al. 2019, ApJ, 877, 104
Zhu, C., Chang, P., van Kerkwijk, M. H., & Wadsley, J. 2013, ApJ, 767, 164